On the Effect of Secondary Nucleation on Deracemization via Temperature cycles

Fabio Cameli[1], Joop H. ter Horst[2], René R. E. Steendam[3], Christos Xiouras[4,], and Georgios D. Stefanidis[1,*]*

[1]Process Engineering for Sustainable Systems (ProcESS), Department of Chemical Engineering KU Leuven, Celestijnenlaan 200F, 3001 Leuven, Belgium.

[2]University of Strathclyde, EPSRC Centre for Innovative Manufacturing in Continuous Manufacturing and Crystallization (CMAC), Strathclyde Institute of Pharmacy and Biomedical Sciences, Technology and Innovation Centre, 99 George Street, Glasgow G1 1RD, United Kingdom.

[3]Ardena, Solid State Research, Meibergdreef 31, 1105 AZ, Amsterdam, Netherlands.

[4]Crystallization Technology Unit (CTU), Janssen Pharmaceutical Companies of Johnson & Johnson, Janssen Research & Development, Tournhoutseweg 30, 2340, Beerse, Belgium.

[*]Corresponding authors: cxiouras@its.jnj.com, georgios.stefanidis@kuleuven.be

Keywords: Chiral resolution, crystal engineering, secondary nucleation, temperature cycling, microwave heating

Abstract

Herein, the pivotal role of secondary nucleation in a crystallization-enhanced deracemization process is reported. During this process, complete and rapid deracemization of chiral conglomerate crystals of an isoindolinone is attained through fast microwave-assisted temperature cycling. A parametric study of the main factors that affect the occurrence of secondary nucleation in this process, namely agitation rate, suspension density and solute supersaturation, confirms that an enhanced stereoselective secondary nucleation rate maximizes the deracemization rate. Analysis of the system during a single temperature cycle shows that while stereoselective particle production during the crystallization stage leads to enantiomeric enrichment, undesired kinetic dissolution of smaller particles of the preferred enantiomer occurs during the dissolution step. Therefore, secondary nucleation is crucial for the enhancement of deracemization through temperature cycles and as such should be considered in further design and optimization of this process, as well as in other temperature cycling processes commonly applied in particle engineering.

Introduction

The need for obtaining enantiopure compounds is widely increasing in fine chemicals manufacturing as well as in pharmaceutical industry.[1] While asymmetric synthesis of a target enantiomer may imply

lengthy protocols, costly catalysts and low product recovery, downstream separations of racemic mixtures offer a valuable and easily applicable alternative for the manufacture of single enantiomers. Among the various purification techniques established so far, chiral resolution via crystallization appears to be the most favorable choice in terms of solid yield (therefore productivity) and operational costs.[1c] A recent striking development in crystallization processes for separating enantiomers are the solid-state deracemization methods[2-3], which feature complete conversion of the unwanted enantiomer to the preferred enantiomer with an unprecedented maximum 100% yield. The solid state deracemization processes are most often realized by applying bead[2b-e] and/or ultrasound grinding[2g-h] or temperature cycling[3] to a racemic suspension of conglomerate crystals in the presence of a liquid-phase racemization reaction. Temperature cycling-induced deracemization (TCID), in which repeated partial dissolution and recrystallization cycles of the chiral species lead to enantiopurity, is perhaps a more promising deracemization approach compared to the bead grinding technique as it circumvents the need for further separation of grinding media from the solid product.[2b]

In TCID, temperature sweeps are applied to a suspension containing racemic conglomerate crystals and a solution in which solute racemization is catalyzed. Although TCID features simple steps in its realization, the key elements of the controlling mechanism of this relatively recent deracemization technique have not been completely established yet. Operating parameters such as the impact of solid mass involved in the thermal cycles,[3b-d] the amount of catalyst,[3c] the cooling rate,[3b,c,e] the suspension volume,[3d-e] the initial enantiomeric excess[3c,e,f], the amplitude of the sweeps,[3c,e,g] the racemization rate,[3h] and the use of additives as growth inhibitors[3i] have been studied previously. Moreover, several computational studies[4] have attributed the observed chiral enrichment to the crystallization step occurring during the cooling stage. The observed increase in chiral enrichment in the solid phase has been ascribed to a difference in the growth rate dispersion between the two enantiomeric crystal size distributions[4a-b] or to a crystal growth mechanism which involves (partial) incorporation of small chiral clusters to crystals of the same chirality.[4c] Another recent publication, which simulates TCID using a population balance model, claims that growth, dissolution and racemization processes alone can explain deracemization without the need for breakage or agglomeration, as long as both temperature and size dependence of solubility (through the Gibbs-Thomson equation) are taken into account.[4d] Indeed, alternative mechanisms to conventional crystal growth following McCabe's ΔL law have been sought to explain deracemization because the latter, featuring equal growth/dissolution kinetics for the different chiral populations, would lead to no changes in enantiomeric enrichment during temperature cycling even in the presence of fast racemization[4a]. Alternatively, the reason for the observed amplification of the enantiomeric excess in TCID might be found in a mechanism related to the bead grinding process in which the presence of small solid enantiopure clusters is deemed responsible for the chiral enrichment. A possible mechanism for the formation of small enantiopure clusters in TCID could be secondary nucleation, which is considered to be the main nucleation mechanism in suspensions.

Secondary nucleation involves the generation of new nuclei facilitated through the presence of particles of the same substance in the suspension.[5] The rate of production of secondary nuclei is mainly dependent on three process parameters, namely agitation intensity, suspension density and solute supersaturation.[5c] Numerous pathways for the generation of secondary nuclei have been discovered[6] and extensively investigated[7] to date. While several studies have highlighted the importance of secondary nucleation in chiral crystallization[8] as early as in the 1950s with the work of Havinga[8c] and later in the work of Kondepudi *et al*.[8d], there is still no clear evidence reported about the interplay between the generation of secondary nuclei and the enantiomeric enrichment in deracemization processes involving thermal cycles. Experimental evidence of secondary nucleation taking place in the recrystallization step during TCID have been reported as secondary nucleation was observed when extremely fast cooling was attained within a microwave apparatus[9] and during stirrer-induced secondary nucleation featuring intense stirring through a homogenizer.[3d] However, previous mechanistic studies on TCID have not considered the effects of secondary nucleation during the cooling/low temperature stage of the process. As such, the exact interplay between the generation of secondary nuclei and the enantiomeric enrichment in deracemization processes involving thermal cycles remains elusive.

Herein, the effect of secondary nucleation on a TCID process is studied experimentally in a microwave apparatus that allows for unprecedented heating and cooling rates. This unique approach enables the dissolution/re-crystallization stages to proceed isothermally at high driving forces. In order to identify potential links between the magnitude of secondary nucleation and the deracemization process, we investigated the effect of three operating parameters that are considered to influence secondary nucleation in stirred crystallization processes, namely agitation rate, suspension density and solute supersaturation. Finally, by comprehensively looking into the evolution of the particle size, liquid phase concentration and solid phase enantiomeric excess of the system during both dissolution and recrystallization stages of the process in just two thermal cycles, we elucidate potential mechanisms which drive TCID. The results of this work advance the understanding into the phenomena involved in deracemization and pave the way towards future industrial applications.

Results

In order to investigate the potential of deracemization for 2-isopropyl-3-hydroxy-3-phenylisoindolin-1-one, **1**, in toluene with catalytic DBU (Scheme 1), a series of batch experiments were carried out at various conditions, reported in Table 1. Prior to the application of temperature cycles, an isothermal experiment (run #1, Table 1) was performed using intense stirring to test whether deracemization is possible even in the absence of temperature cycles. The results of this experiment, reported in ESI, showed no substantial increase in the enantiomeric excess. As expected, in the absence of grinding or temperature cycling, enantiomeric excess does not evolve.

In order to design appropriate temperature profiles for deracemization, the solubility of racemic **1**, in toluene with catalytic DBU (Scheme 1) was measured at various temperatures and reported in Figure 1 (left). The solubility data as a function of temperature can be adequately described by the empirical Equation 1 (*C(T)*; mg $g_{solvent}^{-1}$, *T*; K):

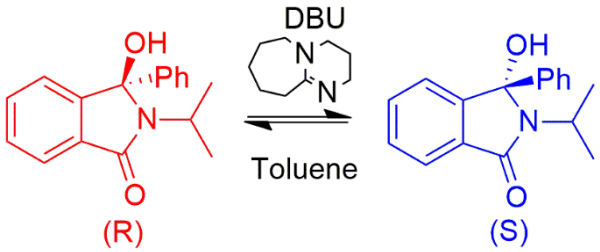

Scheme 1. Racemization reaction of **1** in the presence of catalytic DBU in toluene.

$$C(T) = \exp\left(12.3 - \frac{2868}{T}\right) \quad (1)$$

Based on this information, temperature cycling experiments can be designed featuring different cycle amplitudes ($\Delta T = T_h - T_l$) between the high and low temperatures, T_h and T_l, respectively. In this study, different cycle amplitudes were investigated by keeping T_l the same in all experiments at 35 °C, but varying T_h between 50-80 °C (Figure 1, right). In turn, the amplitude of the thermal cycles dictates the solid mass which dissolves during each cycle, and with that the mass of crystals remaining upon partial dissolution. The theoretical fraction of solid mass after heating at the respective T_h can be quantified according to[3d]:

$$w = \frac{C_t - C^*(T_h)}{C_t - C^*(T_l)} \quad (2)$$

where $C^*(T_h)$ and $C^*(T_l)$ are respectively the equilibrium concentrations of the solution during the isothermal dissolution and crystallization periods and where C_t is the initial total dry mass of crystals used.

Since in this work we were mostly interested in the effect of secondary nucleation on temperature cycling induced deracemization, we focused on studying individually the factors that influence the rate of secondary nucleation during the cooling step, namely agitation rate (runs #2 - #4 in Table 1), supersaturation level (runs #4 - #7 in Table 1) and suspension density (runs #4 and #8 - #11 in Table 1). While the effect of the cooling rate was not investigated in this study, the fastest cooling rate that was experimentally possible was selected in all experiments. Hence, the thermal cycles can be considered to evolve via isothermal dissolution and crystallization stages.

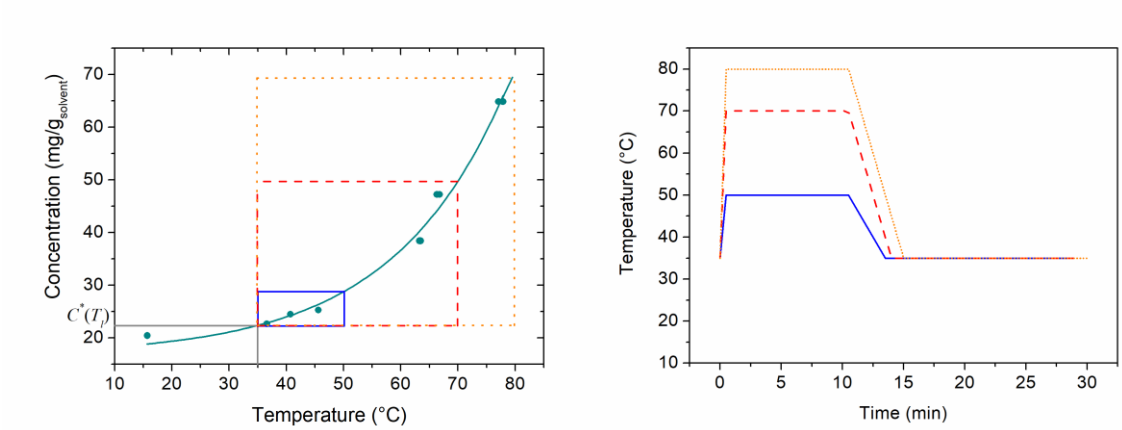

Figure 1. Left: Solubility of rac-**1** in toluene with DBU (33 mM). Solubility limits of the applied cycles with different top temperatures indicated by the blue (T_h = 50 °C), red (T_h = 70 °C) and orange (T_h = 80 °C) lines. The grey line represents the solubility at the low temperature (T_l = 35 °C). Right: Thermal cycles applied with different T_h values and same low temperature limits.

Table 1. Overview of the process conditions during the experiments.

Experimental run #	ΔT (°C)	Supersaturation at T_l = 35 °C S_i (-)	Suspension density at T_h (mg $g_{solvent}^{-1}$)	Agitation rate, N (rpm)	Fraction of mass surviving dissolution, w (%)
1	35	1.0	56.8	1000	100.0
2	35-70	2.6	25.7	550	45.2
3	35-70	2.6	25.7	700	45.2
4	35-70	2.6	25.7	1000	45.2
5	35-50	1.5	25.7	1000	70.6
6	35-80	3.3	25.7	1000	36.4
7	35-90	4.1	0.0	1000	0.0
8	35-70	2.6	6.5	1000	17.4
9	35-70	2.6	16.1	1000	34.1
10	35-70	2.6	63.9	1000	67.2
11	35-70	2.6	73.7	1000	70.3

Effect of agitation rate

A key parameter in establishing the effect of secondary nucleation on a deracemization process employing temperature cycles is the agitation rate through its influence on contact nucleation (collisions between crystal-impeller or crystal-crystal) and fluid shear. In order to investigate qualitatively the extent of secondary nucleation in our system and the influence of the hydrodynamic conditions, we designed three temperature cycling experiments (runs #2 - #4, Table 1), among which the agitation rate is varied between 550 and 1000 rpm. The evolution of the volume-based particle size distributions during these experiments (measured at the end of the temperature cycles) is presented in Figure 2 together with an estimated evolution of the specific surface area per cycle. Note that the specific surface area values were calculated based on the PSDs assuming constant density, spherical non-porous

particles with smooth surfaces and may not quantitatively correspond to the actual specific surface area of the particles at the respective conditions. While these values can only be viewed as indicative, they still provide a helpful means to compare the evolution of the surface area between the different experiments.

The results in Figure 2 reveal that in those experiments, temperature cycling leads to a progressive decrease in crystal sizes and a concomitant increase in the specific surface area. The observed trend in crystal size and specific surface area is ascribed to the formation of secondary nuclei during the crystallization stage. If new particles did not form, the observed trend in size and specific surface area could only be explained by much faster (partial) dissolution compared to crystal growth, which in turn would also lead to a lower suspension density than the theoretical one (based on the solubility at T_l) at the end of each cycle. However, in all experiments the yield at the end of the process was between 91-98% of the theoretical one, with losses pertaining mostly due to filtration. Additionally, the decrease in mean size and increase in specific crystal surface area are more pronounced as the agitation rate (and with that, the secondary nucleation rate) increases form 550 rpm to 1000 rpm. Moreover, while all PSDs exhibit a bimodal trend with several particles < 10 μm, the trend is more pronounced in the case of intense agitation (1000 rpm) with a clear progression of the mean population size towards the small sizes classes, indicating that, as expected, the generation of secondary nuclei is enhanced at higher agitation rates.

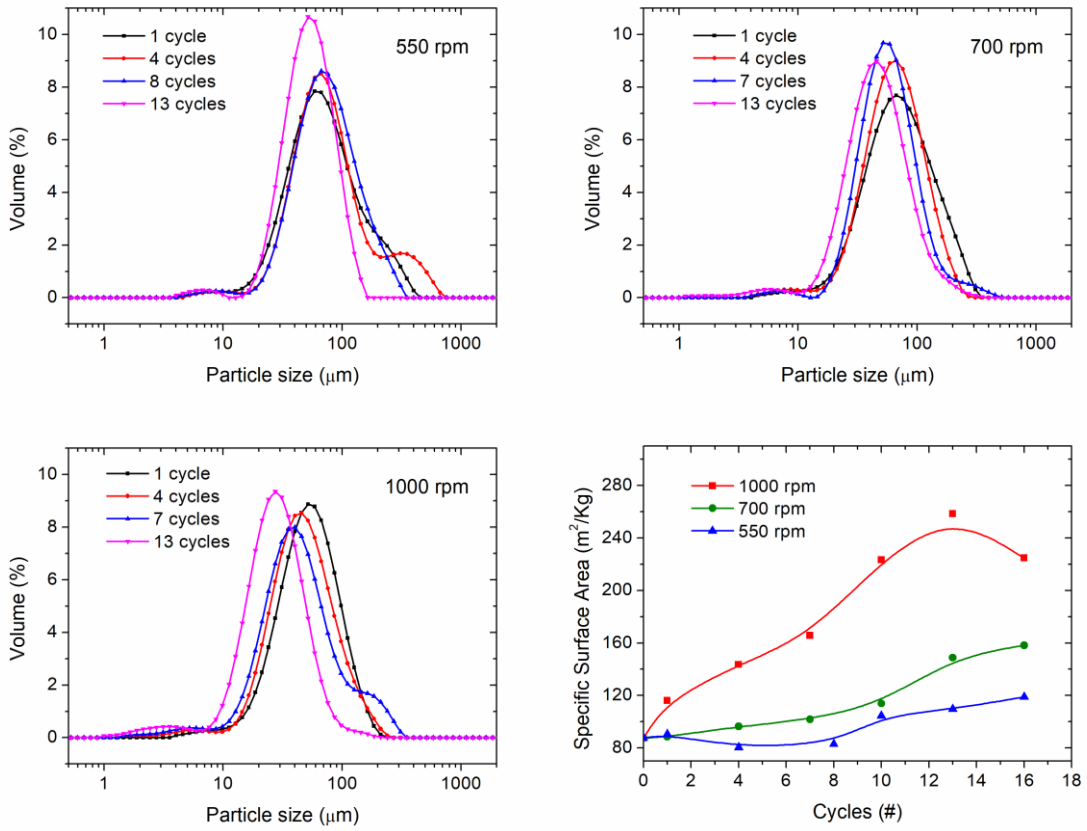

Figure 2. Particle size distributions (PSDs) of temperature cycling experiments with different agitation rates: run #2 (top left), run #3 (top right) and run #4 (bottom left). Bottom right: Estimated evolution of the specific surface area for the same experiments, calculated by the PSDs assuming constant density, spherical non-porous particles with smooth surfaces. Blue triangles, green circles and red squares correspond to runs #2, #3 and #4, respectively.

Furthermore, SEM images (Figure 3) taken after 10 cycles for the three experiments indicate the presence of small particles next to larger ones, which is a typical result of the occurrence of secondary nucleation. Run #4 at 1000 rpm results in the formation of very small particles coexisting with larger ones, in which no substantial signs of mechanical breakage can be detected (Figure 3c). A similar qualitative trend is visible in the pictures featuring the crystals obtained from run #3 at 700 rpm (Figure 3b) and run #2 at 550 rpm (Figure 3a). However, in the latter images it is noticeable that these experimental conditions resulted in larger mean sizes of particles compared to those of run #4, which reflects the data of the PSD shown in Figure 2. The differences in sizes of the small crystals reveal how some of the newly formed nuclei grow larger and may survive the dissolution step.

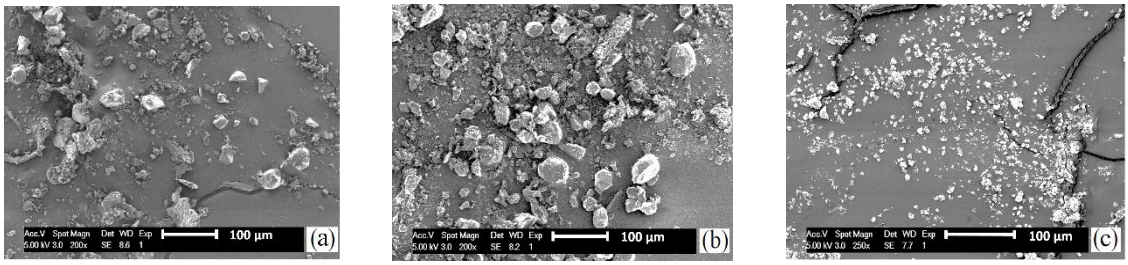

Figure 3. SEM images of crystals at the end of the 10th cycle in runs #2, #3 and #4, at 550 rpm (a), 700 rpm (b) and 1000 rpm (c), respectively.

Figure 4 shows the evolution of the solid phase enantiomeric excess for runs #2 - #4. While all three experiments feature a considerable deracemization rate for TCID processes, resulting in an enantiopure outcome within 16 cycles, a clear trend in the rate of the deracemization can be observed, with an increased agitation rate leading to faster deracemization. It is possible that the faster deracemization rate observed at a higher degree of agitation is linked to the faster production of secondary nuclei in a stereoselective manner. An increase in the agitation rate will introduce secondary nucleation of both enantiomer crystal populations. However the autocatalytic nature of the secondary nucleation process, that sustains the imbalance in enantiomer crystal population (*i.e.* formation of a very large number of secondary nuclei of the same handedness from the surface of a crystal in a stirred solution)[6a,7d-e,8a], ensures that the enantiomeric crystal population in excess will be amplified faster than the minority population. On the other hand, only isothermal stirring cannot deliver enrichment of the chiral suspension via attrition-enhanced deracemization for this system as shown by the isothermal run #1 reported in ESI. In fact, in the absence of any supersaturation, formation of smaller particles must rely

on mechanical breakage, which in our experiments (absence of grinding) is limited. Therefore, the observed trends in Figure 4 cannot be attributed to Viedma ripening[2b].

A deeper study on the evolution of the newly formed secondary nuclei with regards to birth and dissolution along the duration of two thermal cycles is presented in a following section.

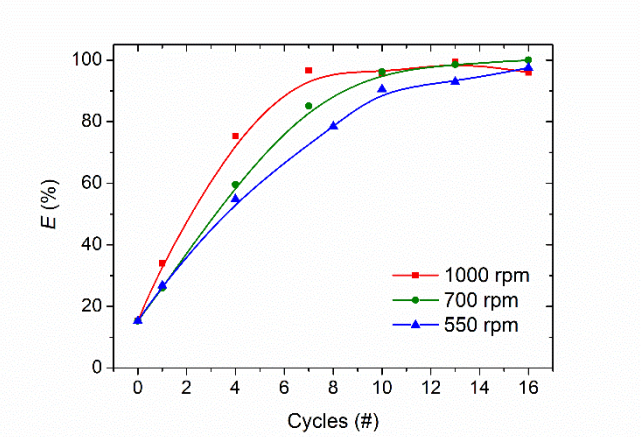

Figure 4. Evolution of the enantiomeric excess *E* for experiments at different agitation rates. Blue triangles, green circles and red squares correspond to runs #2, #3 and #4, respectively.

Effect of supersaturation

In order to study the effect of supersaturation on secondary nucleation during temperature cycling-enhanced deracemization, runs #4 - #6 were performed using different thermal profiles (Figure 1b and Table 1), which in turn induce different supersaturation levels during the crystallization stage at 35 °C. Table 1 reports the supersaturation ratios (S_i) attained at the beginning of the isothermal step at the low temperature, assuming negligible desupersaturation due to nucleation and growth during the fast cooling stage (~2 min for all experiments). As secondary nucleation during crystallization is influenced by both supersaturation and the amount of seed crystals (suspension density), the initial mass of the enantiomers used for runs #4 - #6 was varied to maintain the same suspension density at the end of the partial dissolution phase in each cycle, in order to isolate and study the effect of supersaturation alone. Nevertheless, the undersaturation conditions for dissolution would inevitably change by varying the thermal sweeps, hence affecting possible preferential dissolution of small particles.

The evolution of the enantiomeric excess for runs #4 - #6, is reported in Figure 5 and shows that higher initial supersaturation ratio S_i during the crystallization phase enhances the deracemization rate in the case of sweeps between 35 and 70 °C (red curve) compared to the lower supersaturation ratio attained by running the dissolution stage at 50 °C (blue curve). Indeed, the experiment with sweeps to 70 °C is practically enantiopure after 7 cycles, while the lower supersaturation conditions lead to only 42% enantiomeric excess at the same number of cycles. However, a further increase of the initial supersaturation ratio up to 3.3 (dissolution at 80 °C, orange curve), results in a substantially decreased deracemization rate as compared to the other two experiments. It is also noted that in the extreme case

of S_i = 4.1, enabled by complete dissolution of the crystals at 90 °C (run #7) before cooling, stochastic primary nucleation occurred and no deracemization was observed (ESI).

The observed non-monotonic dependence of the deracemization rate on the initial supersaturation may be a result of the competition between stereoselective and non-stereoselective nucleation occurring via different mechanisms. Although the precise mechanism of secondary nucleation in this system is currently unknown, we can speculate that at lower supersaturation ratios, secondary nucleation originates directly from the seeds through attrition and/or detachment of surface irregularities grown on the seed crystals, thereby leading to the stereoselective production of secondary nuclei and the observed strong enantiomeric enrichment. Obviously, such a mechanism is enhanced by increasing supersaturation, as more attrition fragments form and surface irregularities would grow faster and in a more irregular manner. However, as supersaturation increases further, the concentration and size of subcritical clusters in the solution increases substantially, which after a certain point may lead to non-stereoselective enhanced secondary nucleation through for instance the embryo coagulation mechanism[6b], or even to non-stereoselective primary nucleation, slowing down the deracemization rate. Although this is mainly a hypothesis, evidence of extensive nucleation during the crystallization phase in the high supersaturation experiment (run #6) was indeed observed by the analysis of the PSD evolution reported in ESI together with snapshots of the suspension. The sluggish, slightly irregular evolution of the enantiomeric excess during that experiment, seen in Figure 5, may indicate that multiple nucleation mechanisms that differ in their stereoselective outcomes are simultaneously competing for the consumption of the supersaturation. A similar dependence of the mechanism and stereoselective outcome of secondary nucleation on supersaturation was also reported in the work of Denk and Botsaris for sodium chlorate[5a].

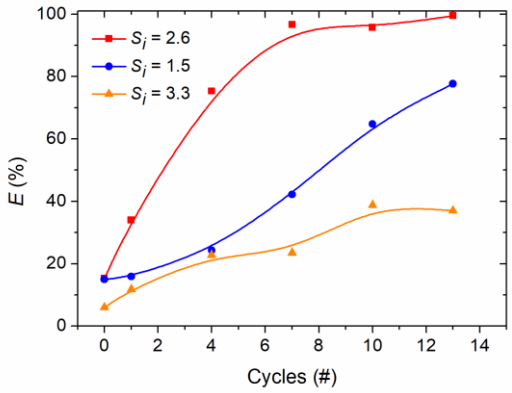

Figure 5. Enantiomeric excess (E) trend for experiments run under different initial supersaturations (S_i), but with the same suspension density at the beginning of the cooling stage. Red squares, blue circles and orange triangles correspond to runs #4, #5 and #6, respectively.

Effect of suspension density

The third key parameter for secondary nucleation in TCID is the suspension density at the initial stages of the crystallization phase, as contact nucleation through the collision among particles or with the stirrer is deemed as one of the most effective routes for the generation of new crystals. Additionally, shear-induced secondary nucleation is also assumed to benefit from the higher crystal surface area provided by increasing suspension density. In fact, contact among particles is inevitable in agitated suspensions and can induce detachment of surface irregularities growing on top of larger crystals as well as the displacement of the coagulated solute layer at the solution side of the surface of the parent crystal. Figure 6 presents the deracemization trend of run #4 and runs #8 - #11 performed under the same temperature profile and thus the same initial supersaturation during the crystallization phase, but with different values for the initial suspension density at the beginning of the crystallization step. As compared to run #4 at 25.7 mg $g_{solvent}^{-1}$, run #8 at 6.5 mg $g_{solvent}^{-1}$ showed a slower deracemization rate from the early cycles and a subsequent decline in the solid-state enantiomeric excess, which is likely due to the formation of crystals of both chiralities. This behavior might be a consequence of a low suspension density during the start of the crystallization stage as the fraction of mass dissolved per cycle is higher than the other cases. The relatively small amount of crystals left after the dissolution stage (mass fraction surviving dissolution, *w*, is only 17.4% in run #8, as compared to 45% in run #4) cannot consume the applied supersaturation through stereoselective secondary nucleation alone. Instead, non-stereoselective nucleation and/or primary nucleation also occur, leading to the formation of both chiral forms and a decrease in enantiomeric excess. The observed increase in number of particles during application of thermal cycles for run #8 is reported in ESI. Hence, a threshold suspension density exists below which non-stereoselective secondary nucleation takes place in addition to stereoselective secondary nucleation. Such a threshold suspension density was also found for sodium bromate[3d] and is expected to be system dependent.

On the other hand, increasing the suspension density up to 63.9 mg $g_{solvent}^{-1}$ (runs #4, #9 and #10) does not significantly influence the observed behavior of the enantiomeric excess: the deracemization rate as a function of suspension density reaches a plateau value. Taking into account that at a higher suspension density more solid mass is required to be deracemized whilst the thermal sweeps involve the same quantity of crystal mass, it can be concluded that a higher suspension density results in enhanced specific deracemization rate [% chiral enrichment / (number of cycles × suspension density)]. Moreover, given that the same amount of solvent is employed in these experiments, it can be concluded that higher suspension density results in enhanced process productivity in terms of mass of target enantiomer delivered per unit of time. Under these conditions of increasing suspension density, the deracemization rate must be enhanced by the larger magnitude of secondary nucleation, which balances the drawback of involving the same absolute amount of mass in the thermal sweeps. Besides, the relatively low percentage of mass dissolved in each cycle at high suspension densities could favor the

survival of the freshly formed nuclei of the preferred enantiomer, which can further boost stereoselective secondary nucleation in the subsequent cycle.

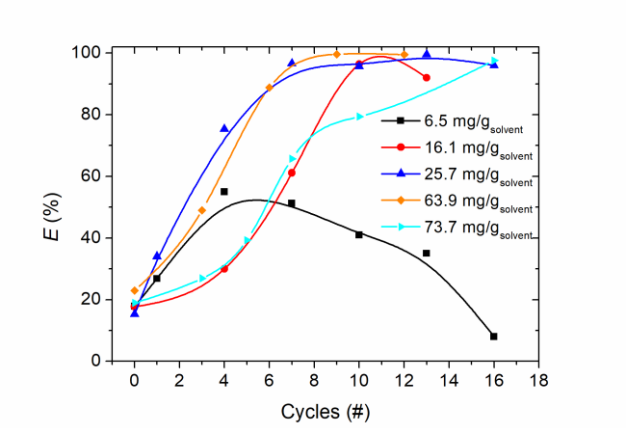

Figure 6. Enantiomeric excess *E* as a function of the number of temperature cycles for different suspension densities. Blue triangles, black squares, red circles, orange rhombi and cyan inverted triangles, correspond to runs #4 and #8 - #11, respectively.

However, by further increasing the suspension density up to 73.7 mg $g_{solvent}^{-1}$ in run #11, the deracemization rate does not increase further, but instead it is found to decrease. An increase in suspension density also leads to a larger amount of solids to be deracemized. This effect leads to a decrease in deracemization rate and counterbalances the effect of secondary nucleation, thus making suspension density a valuable process parameter required for future process modelling of TCID systems.

Thus, the suspension density strongly dictates the deracemization rate as it controls the balance between the different mechanisms taking place. At too low suspension densities, non-stereoselective processes may occur which lead to inhibition of deracemization. At too high suspension densities, the amount of solid material to be deracemized is large and requires a long deracemization time.

Investigation into a single temperature cycle

All measurements reported so far referred to the low temperature isothermal stage of the thermal cycles. Monitoring the behavior of the system during the heating, cooling and high-temperature phases can prove helpful in understanding the phenomena leading to enantiomeric enrichment. Usually this is not possible, as for most compounds and temperature profiles, the changes in the enantiomeric excess obtained in a single cycle are very small and thus difficult to detect. However, this is not a limitation in the present work as appreciable deracemization occurs during a single temperature cycle. Thus, the evolution of the populations of the two enantiomeric crystals over just two temperature cycles is an efficient means to understand how the enantiomeric enrichment unfolds and which physical phenomena are controlling it.

In order to investigate the behavior of the system during the various stages of the temperature cycle, two-cycle experiments were run between 35 and 70 ºC and an agitation rate of 1000 rpm with additional intermediate sampling during the isothermal holding steps at T_h and T_l. Figure 7 shows the evolution of the solid phase enantiomeric excess for different experiments featuring different values of the initial enantiomeric excess (E_0=0.5, 21 and 41%) and equal value of suspension density at the end of the dissolution stage (25.7 mg $g_{solvent}^{-1}$). As expected, for the experiments featuring a higher E_0, E exhibits a pronounced non-monotonic behavior during a single cycle, with a steep increase during the dissolution step and a more constant period during the crystallization step. Notably, no decrease in the enantiomeric excess is observed during the crystallization step, even though the total mass is increasing, which illustrates that the mass of the excess enantiomer increases faster than that of the counter enantiomer.

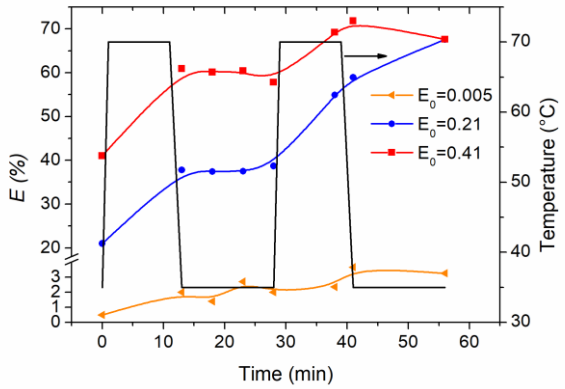

Figure 7. Evolution of the enantiomeric excess (E) in the various stages of the temperature cycling process for three experiments featuring different initial enantiomeric excesses (orange curves with triangles correspond to an initial excess of 0.5%, blue curves with circles feature an initial excess of 21% while the initial enantiomeric excess of the red curves with squares was 41%. In all cases w is equal to 45.2%. Black line refers to the applied temperature profile. All the experiments were run at 1000 rpm.

In order to obtain additional insight into the behavior of the system during the two cycles, the enantiomeric excess data of Figure 7 are combined with independent estimates of the total mass of the crystals (estimated by a mass balance using liquid phase concentration measurements at the same times) to obtain the total crystal mass concentration of R and S species during the isothermal dissolution and crystallization steps for the different experiments (Figure 8, left). The results indicate that when the two enantiomeric crystal populations are very similar in mass (*i.e.* E_0=0.5%) at the beginning of the experiment, they evolve almost symmetrically over the dissolution and crystallization phases leading to only small enantiomeric enrichment. This implies that in the dissolution stage the two enantiomers dissolve equimolarly as expected for a conglomerate-forming compound. Similarly, the crystallization

phase is not significantly biased towards one chiral species yielding the close trends of *R* and *S* crystal concentrations represented by the orange curves in Figure 8 (left).

Conversely, when a significant mass imbalance is present in the initial chiral mixture of the enantiomeric crystal populations, crystal dissolution no longer proceeds in an equimolar fashion, which becomes apparent in the two stages of dissolution at high temperature reported in Figure 8 left (blue and red curves). Relatively more mass of the excess enantiomer (*R* species in this case) dissolves compared to the *S* enantiomer. In the experiment with E_0=21%, the crystal mass of *R* which dissolves at a high temperature is 1.7 times higher than the mass of *S* while in the case of E_0=41%, 3.2 times more of the *R* enantiomer crystals dissolve. These amounts very roughly correspond to the ratio of the enantiomer masses at the start of the two processes (1.53 and 2.4, respectively). Thus, neglecting the possible differences in the PSDs of the two enantiomers, we assume that the non-equimolar dissolution is attributed to kinetic dissolution of the preferred enantiomer that is present in a larger amount and thus possesses a larger available surface area for dissolution. Once the preferred enantiomer dissolves first, the fast racemization reaction converts it to the counter enantiomer maintaining the driving force for dissolution equal for each enantiomer. However, it is worth mentioning that even though undesired conversion of the preferred enantiomer to the counter enantiomer may occur during the dissolution phase, the overall enantiomeric excess can still increase (evidently from 39% to 55% and from 58% to 69%, for the two experiments, as visible in the second cycle), since the total solid mass (m_R + m_S) decreases more than the difference between the enantiomer solid masses (m_R - m_S). Hence, the dissolution process contributes substantially in the increase of the enantiomeric excess during deracemization by temperature cycles even when it is biased toward the preferred enantiomer.

During the cooling and isothermal holding steps at the lower temperature, for the same experiments at higher initial enantiomeric excess (blue and red curves in Figure 8 left), both enantiomers crystallize leading to an increase in the suspension density of both chiral crystalline phases, with the average rate of mass increase of the enantiomer in excess being higher during that period. In fact, when only 0.5% initial enantiomeric excess is employed, the solid mass increase of the preferred enantiomer is only 4% higher than the counter enantiomer, while in the experiment with E_0=41%, 77% of the crystallized mass is of the target enantiomer. Thus, the autocatalytic nature of the crystallization process becomes apparent when the mass imbalance between the two enantiomers is higher at the start of the isothermal step at low temperature. It is worth pointing out that this value refers only to the isothermal crystallization step, although part of the crystallization must take place also during the fast cooling stage (~2 min), in which it is assumed that a similar trend in enantioselective crystallization is present. Furthermore, it is apparent from the different trends in Figure 8a that the main portion of the crystallizing mass appears at the beginning of the crystallization period, when the supersaturation is higher and then follows an asymptotic behavior until the end of the isothermal period.

This large increase in the difference between the mass of the enantiomers in the crystallization stage of the temperature cycle may be explained by the occurrence of stereoselective secondary nucleation. Figure 8b shows the evolution of the specific surface area of both enantiomers for the same experiments, measured by laser diffraction. For every experiment, the specific surface area constantly increases during the crystallization stage, which confirms the occurrence of secondary nucleation, since a purely growth-dominated crystallization would lead to the opposite behavior, *i.e.* a decrease in the specific surface area. Furthermore, the values of specific surface area calculated from laser diffraction greatly underestimate the presence of fines and surface defects that could play a central role during the crystallization process. Conversely, during the dissolution stage the specific surface area decreases, which indicates the disappearance of some of the smaller particles formed during the crystallization stage. While the increase in the specific surface area (and thus the generation of secondary nuclei) appears similar during the crystallization stage for the three experiments, the handedness of the secondary nuclei, as shown in Figure 8a, which in turn dictates the enrichment achieved in a single cycle, heavily depends on the amounts of the two enantiomers that seed the crystallization process in each step. Hence, higher enantiomeric imbalance at the beginning of the crystallization stage results in more secondary nuclei of the excess chirality produced.

In Figure 9, it is shown that in the extreme case where all the particles undergoing temperature cycling are of one handedness, the formation of new particles (as indicated by the slightly increasing specific surface area) unfolds only through stereoselective secondary nucleation, as the chirality of the particles remained the same throughout the process. This conclusion must hold for supersaturation conditions that do not prompt non-stereoselective nucleation as observed in Figure 5. Thus, the trend displayed in Figure 9 highlights the importance of the chiral bias represented by the enantiomeric seeds that seemingly steer the stereoselective formation of new particles. Therefore, the same mechanism must govern the chiral enrichment in Figure 8a, in which the experiments featuring a higher spread between the two chiral populations deliver higher deracemization rate through autocatalytic formation of secondary nuclei.

Besides, as the specific surface area is inversely proportional to the mean particle diameter, partial dissolution of the crystals would lead to an increase of the specific surface area as in the case shown in Figure 9. Therefore, the dissolution phase for the enantiopure particles, that featured similar sizes among each other, mainly resulted in crystal shrinkage rather than kinetic dissolution of small particles as in the experiments displayed in Figure 8b. A more detailed representation of the specific surface area distribution for these experiments, reported in ESI, shows that the dissolution step yields significant dissolution of small particles generated in the crystallization phase for the experiments starting with scalemic conditions.

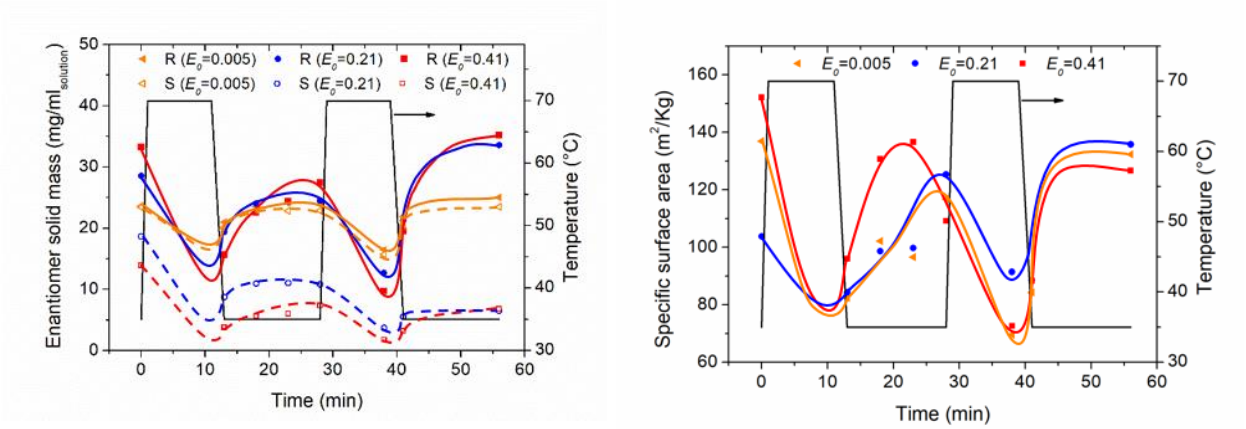

Figure 8. Left: Evolution of the crystal mass concentration of the *R* enantiomer (solid lines, full symbols) and *S* enantiomer (dashed curves, empty symbols) during two thermal sweeps. Different initial enantiomeric excesses of the *R* form were employed: orange curves with triangles correspond to an initial excess of 0.5%, blue curves with circles feature an initial excess of 21% while the initial enantiomeric excess of the red curves with squares was 41%. Right: Trend of the total (*R* + *S*) specific surface area during two thermal sweeps for the same experiments. Lines are drawn as a guide to the eye. Black lines represent the applied temperature profile.

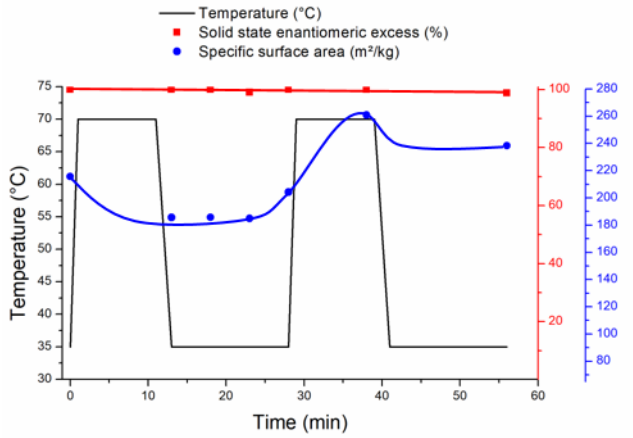

Figure 9. Enantiomeric excess (red squares) and specific surface area values (blue circles) of an initially enantiopure suspension during the application of two temperature cycles. Lines are drawn as a guide to the eye.

Discussion

The results presented in this work indicate that stereoselective secondary nucleation occurs during the cooling/isothermal stage of a temperature cycling-enhanced deracemization process. Furthermore, the magnitude of secondary nucleation seems to directly influence the deracemization rate, with higher secondary nucleation rates leading to faster deracemization. Although the operating conditions of our experiments can be viewed as quite extreme (thermal sweeps of ± 35 °C at ~ 18 °C min^{-1}), thereby favoring secondary nucleation, we believe that the occurrence of the latter process cannot be excluded in other systems reported in the literature employing temperature cycling for deracemization at milder

conditions. For example, in the study of Suwannasang *et al.*[3g], wherein deracemization of a chiral compound was performed employing temperature cycles at a maximum of ± 10 °C and very slow cooling rates in the order of ~0.2 °C min^{-1}, it was shown by SEM microscopy that in many experiments the particle size progressively reduced after application of temperature cycling, similar to our results. A possible explanation to this observation could be the formation of small particles due to secondary nucleation. It is noted that in the absence of new particle formation, temperature cycling should in principle affect a population of crystals similar to Ostwald ripening, *i.e.* increase in the mean population size and decrease in the number of particles.

Indeed, the secondary nucleation threshold (SNT), *i.e.* threshold supersaturation below which secondary nucleation is negligible, can in certain systems/operating conditions be extremely low[5b], while contact secondary nucleation often requires a surprisingly small impact energy to be effective.[7d,10] Coupled with the fact that most temperature cycling deracemization experiments were performed in small scale equipment using magnetic stirring bars, the probability for secondary nucleation may be considered high even at seemingly mild conditions (small amplitude of temperature cycles and/or cooling rates). Indeed, in larger crystallizers, contact nucleation is less efficient and it was observed that under those conditions, temperature cycling alone was not sufficient to deracemize sodium bromate[3d]. For sodium bromate it was required to have a sufficiently high suspension density which would avoid non-stereoselective nucleation. A high suspension density was previously realized through crystal breakage with the use of a homogenizer. In the present work, a high suspension density was maintained through secondary nucleation which was induced through rapid cooling. However, in the present study it was also shown that some of the secondary nuclei of the preferred enantiomer formed in excess during the crystallization step, being significantly smaller than the crystals of the counter enantiomer, may dissolve preferentially in the dissolution step. To alleviate this undesired effect, one could homogenize (*e.g.* by wet-milling) the crystals prior to the dissolution phase in order to bring the size of the larger counter enantiomer crystals closer to the size of the newly-formed crystals of the preferred enantiomer. Unfortunately, such apparatus is unsuitable for the small microwave cavity employed in this study.

Among the operating parameters affecting the rate of secondary nucleation, solute supersaturation and suspension density have proven to affect the deracemization rate in a non-monotonic fashion, whereas increasing agitation intensity proportionally enhances deracemization rate. An overview of the effect of solute supersaturation and suspension density on the deracemization rate per cycle is shown in Figure 10, where one could ideally find optimal values of the process parameters to achieve the highest deracemization rate. The values for the deracemization rate were obtained through linear fits of the enantiomeric excess vs. number of cycles data. It is seen from Figure 10 that deracemization rates between 10.7 and 11.6 % per cycle are obtained when supersaturation ratio is equal to 2.6 and suspension density varies between 25.7 and 63.9 mg $g_{solvent}^{-1}$. Beyond these operating limits, decreased deracemization rates per cycle are observed with the lowest value of 2.5% per cycle detected for the

case of supersaturation ratio of 3.3 and suspension density of 25.7 mg $g_{solvent}^{-1}$. Therefore, for this specific system, the set of operational parameters that delivered the highest deracemization rate (11.6 % per cycle) comprises of suspension density at high temperature of 25.7 mg/$g_{solvent}$, solute supersaturation ratio of 2.6 and agitation rate equal to 1000 rpm. It is worth pointing out that in the present study the influence of the racemization kinetics on the deracemization process was not investigated. However, as shown previously[3h], the latter can also be an important factor for optimizing deracemization by temperature cycles.

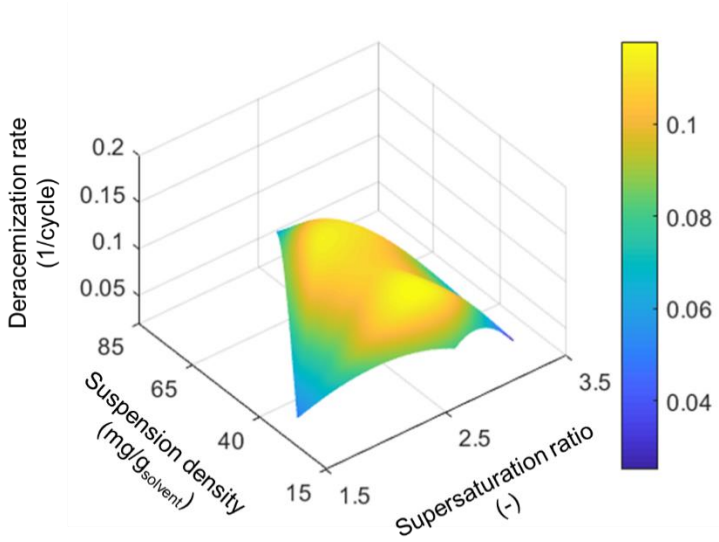

Figure 10. Effect of increasing suspension density and solute supersaturation ratio on the cycle-based deracemization rate.

Currently, secondary nucleation has not been incorporated in the proposed process models that attempt to capture the mechanisms behind deracemization via temperature cycles[4]. The present work demonstrates that stereoselective secondary nucleation is a key feature of temperature cycling-enhanced deracemization and the deracemization pathway is therefore similar to Viedma ripening[2b] since both processes rely on continuous surface area formation through the generation of new particles in a stereoselective manner (through particle breakage in Viedma ripening and stereoselective secondary nucleation in temperature cycling). However, since preferential dissolution of the small secondary nuclei of the preferred enantiomer can occur, an additional nuclei survival mechanism may be required for complete deracemization. Although not yet experimentally verified, such a mechanism could be an enantioselective agglomeration phenomenon, as proposed for Viedma ripening, in which secondary nuclei are incorporated in the larger crystals during the growth stage of the cycle in parallel to secondary nucleation.[11]

Conclusions

In conclusion, we achieved complete and rapid solid-state deracemization of a chiral isoindolinone by microwave-assisted temperature cycling under conditions which strongly favor the occurrence of

secondary nucleation. The effect of secondary nucleation on deracemization by temperature cycles was elucidated by studying the effects of operating parameters that are linked with the generation of secondary nuclei in seeded crystallization processes, namely agitation rate, suspension density and solute supersaturation. Careful measurements of the evolution of the particle size and enantiomeric excess during these experiments reveals that an increase in the agitation rate results in the enhancement of stereoselective secondary nuclei formation, which in turn leads to an enhanced deracemization rate. An increase in either supersaturation at a constant suspension density or an increase in suspension density at constant supersaturation during the isothermal stages at low temperatures also leads to an increase in deracemization rate initially. Interestingly, this effect reverses upon exceeding a threshold value of the supersaturation or suspension density. In the first case, non-stereoselective nucleation lowers the enantiomeric enrichment at high solute supersaturation ratios, whilst high suspension density levels imply lower percentage of mass involved in the dissolution/crystallization cycles thus lower deracemization capacity. Finally, a close inspection of the behavior of the system over the duration of just two temperature cycles for various experiments reveals that both dissolution and re-crystallization are heavily biased towards the enantiomer in excess, with re-crystallization being the most important factor for chiral enrichment achieved during a single cycle. Since the presence of secondary nucleation is seemingly beneficial for this process, it would be relevant to investigate the emergence of secondary nucleation in other more common systems (at milder conditions) in order to assess the system specificity of the findings of this work and subsequently focus on the optimization of such phenomenon, if it is proven to be indeed a general leading mechanism in temperature cycling-induced deracemization.

Experimental section

Materials

2-isopropyl-3-hydroxy-3-phenylisoindolin-1-one, **1**, was synthesized following the procedure reported in ESI. The experimental conditions for deracemization were chosen on the basis of previous successful attempts of solid state deracemization of **1** via attrition-enhanced deracemization[12,13]. These process conditions included 3 mL of toluene (Alfa Aesar), 15 μL of catalytic racemization agent 1,8-diazabicyclo[5.4.0]undec-7-ene (DBU, Sigma Aldrich) and 200 mg (unless otherwise stated) of crystalline **1**.

Solubility measurements

The temperature-dependent solubility of **1** in toluene with catalytic amounts of DBU (same concentration as in the deracemization experiments) was obtained by clear point measurements at various concentrations by adding a known amount of racemic 1 in 0.872 g of toluene and DBU in a 1.5 mL vial. The solubility in the absence of the catalyst was also measured via gravimetric analysis (reported in ESI) showing an overall lower solubility of **1** in pure toluene over temperature as compared

to the case including DBU. The vials were placed in a Crystal16 apparatus (Technobis, Crystallization Systems) and three consecutive temperature cycles were applied to all vials. Each cycle consisted of heating the suspension to 90 °C at 0.2 °C min^{-1}, holding at 90 °C for 10 min, cooling to 0 °C at 5 °C min^{-1} and holding at 0 °C for 2 h. For each cycle, the saturation temperature was recorded for each vial as the temperature at which 100% transmissivity of the detecting laser was achieved.

Temperature cycling experiments

All deracemization experiments were performed in a microwave reactor (Anton Paar Monowave 300), which allows for both rapid heating via microwave irradiation and fast cooling through a jet of compressed air (5 bar) into the microwave cavity. During the experiments, the internal suspension temperature was measured and controlled by an optical fiber probe, while the reactor wall temperature was measured by an IR sensor. In all experiments, the low temperature of the cycle (T_l) was kept the same (35 °C), while the high temperature (T_h) was varied between 50-80 °C. The suspension was agitated throughout the experiments with an oval-shaped magnetic stirring bar (ø=0.5 cm, L=1 cm), stirring at constant values between 550 and 1000 rpm.

Sampling

In most experiments, samples of the suspension were taken at the end of the cycles (i.e. at the end of the isothermal crystallization stage). For some experiments, samples were also taken at intermediate stages of the isothermal dissolution and crystallization stages of the thermal cycles. In every sampling event, 100 µL of the suspension was withdrawn from the reactor and filtered on a glass filter (Porosity 5, ø=1-1.6 µm) to separate the solid from the liquid phase and both phases were subjected to analysis. After the end of the experiments, the overall solid mass retrieved by filtering the samples was used to calculate the total solid yield (Y) defined as the total mass collected from the process over the theoretical mass available at the cold stage of the temperature cycles:

$$Y = \frac{M_s}{M_0 - C^*(T_l) * m_{solvent}} \quad (3)$$

Where M_s is the total mass collected by filtration, M_0 is the initial dry mass of crystals, $C^*(T_l)$ is the solubility at the low temperature step expressed in mg $g_{solvent}^{-1}$ and $m_{solvent}$ is the total mass of solvent employed.

Solid and liquid phase characterization

The solid phase enantiomeric excess (*E*) of the dried crystals was determined by chiral HPLC analysis after dissolution in 2-propanol. The enantiomers of **1** were separated by a Lux Amylose-1 (Phenomenex) column running at 0.5 mL min^{-1} of a mixture of *n*-hexane/ethanol 95/5 (v/v%). After separation, the enantiomers were subsequently detected by a Diode Array Detector (DAD) at a wavelength of 254 nm (retention times: 16 min for R and 20 min for S). The enantiomeric excess was

quantified as the relative difference between the areas of the integrated peaks displayed in the chromatograms: $E = \frac{|A_R - A_S|}{A_R + A_S}$ where A_R and A_S represent the areas of the integrated curves respectively for the *R* and *S* enantiomers. Therefore, from the enantiomeric excess trend an estimation of the deracemization rate per unit of cycle [% chiral enrichment / number of cycles] can be calculated to compare the different experiments. This definition equals a time-based deracemization rate as the cycle duration remains constant in all the experiments while a specific deracemization rate [% chiral enrichment/ (number of cycles * suspension density)] can be introduced when the suspension density varies in the experiments. Additionally, part of the dried crystals withdrawn from the suspension was subjected to particle size analysis by laser diffraction (Malvern 3000, Mastersizer), in order to determine the crystal size distribution (CSD) of the sample, which was assumed to be representative of the whole crystal population in the reactor. *n*-hexane was used as a dispersant in a Hydro SV cell of a Malvern Mastersizer 3000 laser diffractometer. A magnetic stirring bar (1800 rpm) was used to ensure dispersion of the crystals and to avoid agglomeration without inducing crystal breakage. The absence of crystal breakage during the measurements was ascertained by monitoring the obscuration (percentage of laser intensity decrease after passing through the particle field), which remained essentially constant during the duration of the measurements. In some experiments, the liquid phase concentration of **1** was also measured via UV-Vis analysis (Lambda 365, Perkin Elmer) by firstly producing a calibration curve that linked values of known solute concentrations with absorbance levels recorded by the instrument at the same conditions as the experiments.

Acknowledgement

This project has received funding from the European Union's Horizon 2020 research and innovation programme under the Marie Skłodowska-Curie grant agreement No 721290. This publication reflects only the author's view, exempting the Community from any liability. Project website: http://cosmic-etn.eu/. Fabio Cameli thanks Prabhat Ranjan for synthesizing the compound used in the experiments. J.H.t.H. thanks the EPSRC Centre for Innovative Manufacturing in Continuous Manufacturing and Crystallization (http://www.cmac.ac.uk) for support (EPSRC funding under Grant Reference: EP/I033459/1).

References

[1] a) E. Francotte, W. Lindner, *Chirality in Drug Research*, VCH, Weinheim, **2006**. b) J.-F. C. Guo-Qiang Lin, Qi-Dong You, *Chiral Drugs. Chemistry and Biological Action*, John Wiley & Sons, Inc., Hoboken, New Jersey, **2011**. c) H. Lorenz, A. Seidel-Morgenstern, *Angew. Chem. Int. Ed.* **2014**, *53*, 1218–1250.

[2] a) C. Rougeot, J. E. Hein, *Org. Process Res. Dev.* **2015**, *19*, 1809–1819. b) C. Viedma, *Phys. Rev. Lett.* **2005**, *94*, 3–6. c) C. Viedma, B. J. V Verkuijl, J. E. Ortiz, T. De Torres, R. M. Kellogg, D. G. Blackmond, *Chem. Eur. J.* **2010**, *16*, 4932–4937. d) W. L. Noorduin, W. J. P. Van

Enckevort, H. Meekes, B. Kaptein, R. M. Kellogg, J. C. Tully, J. M. Mcbride, E. Vlieg, *Angew. Chem. Int. Ed.* **2010**, *49*, 8435–8438. e) W. L. Noorduin, H. Meekes, A. A. C. Bode, W. J. P. Van Enckevort, B. Kaptein, R. M. Kellogg, E. Vlieg, *Cryst. Growth Des.* **2008**, *8*, 1675–1681.f) C. Xiouras, E. Van Cleemput, A. Kumpen, J. H. Ter Horst, T. Van Gerven, G. D. Stefanidis, *Cryst. Growth Des.* **2017**, *17*, 882–890. g) C. Xiouras, A. Fytopoulos, J. Jordens, A. G. Boudouvis, T. Van Gerven, G. D. Stefanidis, *Ultrason. Sonochem.* **2018**, *43*, 184-192. h) C. Xiouras, A. Fytopoulos, J. H. Ter Horst, A. G. Boudouvis, T. Van Gerven, G. D. Stefanidis, *Cryst. Growth Des.* **2018**, *18*, 3051-3061. i) C. Xiouras, J. H. Ter Horst, T. Van Gerven, G. D. Stefanidis, *Cryst. Growth Des.* **2017**, *17*, 4965-4976.

[3] a) C. Viedma, P. Cintas, *Chem. Commun.* **2011**, *47*, 12786. b) K. Suwannasang, A. E. Flood, C. Rougeot, G. Coquerel, *Cryst. Growth Des.* **2013**, *13*, 3498–3504. c) W. W. Li, L. Spix, S. C. A. De Reus, H. Meekes, H. J. M. Kramer, E. Vlieg, J. H. Ter Horst, *Cryst. Growth Des.* **2016**, *16*, 5563–5570. d) R. R. E. Steendam, J. H. ter Horst, *Cryst. Growth Des.* **2018**, *18*, 3008–3015. e) F. Breveglieri, G. M. Maggioni, M. Mazzotti, *Cryst. Growth Des.* **2018**, *18*, 1873–1881. f) G. M. Maggioni, M. P. Fernández-Ronco, M. van de Meijden, R. M. Kellogg, M. Mazzotti, *CrystEngComm.* **2018**, *20*, 3828–3838. g) K. Suwannasang, A. E. Flood, C. Rougeot, G. Coquerel, *Org. Process Res. Dev.* **2017**, *21*, 623–630. h) R. Oketani, M. Hoquante, P. Cardinael, G. Coquerel, *Cryst. Growth Des.* **2018**, *18*, 6417–6420. i) G. Belletti, H. Meekes, F. P. J. T. Rutjes, E. Vlieg, *Cryst. Growth Des.* **2018**, *18*, 6617–6620.

[4] a) K. Suwannasang, G. Coquerel, C. Rougeot, A. E. Flood, *Chem. Eng. Technol.* **2014**, *37*, 1329–1339. b) R. Uchin, K. Suwannasang, A. E. Flood, *Chem. Eng. Technol.* **2017**, *40*, 1252–1260. c) H. Katsuno, M. Uwaha, *Phys. Rev. E* **2016**, *93*, 1–10. d) B. Bodák, G. M. Maggioni, M. Mazzotti, *Cryst. Growth Des.* **2018**, *18*, 7122−7131.

[5] a) E. G. Denk, G. D. Botsaris, *J. Cryst. Growth.* **1972**, *14*, 493–499. b) T. L. Threlfall, S. J. Coles, *CrystEngComm.* **2016**, *18*, 369-378. c) S. G. Agrawal, A. H. J. Paterson, *Chem. Eng. Commun.* **2015**, *202*, 698–706.

[6] a) R. Y. Qian, G. D. Botsaris, *Chem. Eng. Sci.* **1998**, *53*, 1745–1756. b) R. Qian, G. D. Botsaris, *Chem. Eng. Eng. Sci.* **1997**, *52*, 3429–3440. c) E. G. Denk, G. D. Botsaris, *J. Cryst. Growth.* **1972**, *15*, 57–60.

[7] a) Y. Cui, A. S. Myerson, *Cryst. Growth Des.* **2014**, *14*, 5152–5157. b) M. L. Briuglia, J. Sefcik, J. H. Horst, *Cryst. Growth Des.* **2019,** *19***,** 421−429 c) R. R. E. Steendam, P. J. Frawley, *Cryst. Growth Des.* **2019**, *19*, 3453−3460. d) J. Anwar, S. Khan, L. Lindfors, *Angew. Chem. Int. Ed.* **2015**, *54*, 14681–14684. e) A. Cacciuto, S. Auer, D. Frenkel, *Nature*. **2004**, *428*, 404–406.

[8] a) M. McBride, R. L. Carter, *Angew. Chem. Int. Ed. Engl.* **1991**, *30*, 293–295. b) J. Cartwright, J. García-Ruiz, O. Piro, C. Ignacio Sainz-Díaz, I. Tuval *Phys. Rev. Lett.* **93**, 035502. c) E. Havinga, *Biochim. Biophys. Acta*. **1954**, *13*, 171–174. d) D. K. Kondepudi, R. J. Kaufman, N. Singh, *Science*. **1990**, *250*, 975–976.

[9] F. Cameli, C. Xiouras, G. D. Stefanidis, *CrystEngComm.* **2018**, *20*, 2897.

[10] R. W. Rousseau, F. P. O'Dell, *Ind. Eng. Chem. Process Des. Dev.* **1980**, *19*, 603–608.

[11] M. Mcbride, J. C. Tully, *Nature*, 2008, *452, 161-162*..

[12] F. Yagishita, H. Ishikawa, T. Onuki, S. Hachiya, T. Mino, M. Sakamoto, *Angew. Chem. Int. Ed.* **2012**, *51*, 13023–13025.

[13] R. R. E. Steendam, M. C. T. Brouwer, E. M. E. Huijs, M. W. Kulka, H. Meekes, W. J. P. Van Enckevort, J. Raap, F. P. J. T. Rutjes, E. Vlieg, *Chem. Eur. J.* **2014**, *20, 13527–13530*.